

Formation of mitochondrial-derived vesicles is an active and physiologically relevant mitochondrial quality control process in the cardiac system

Virgilio J. J. Cadete¹, Sonia Deschênes¹, Alexanne Cuillerier¹, François Brisebois¹, Ayumu Sugiura², Amy Vincent⁴, Doug Turnbull⁴, Martin Picard³, Heidi M. McBride² and Yan Burrelle¹

¹Faculty of Pharmacy, Université de Montréal, Montréal, Québec, Canada

²Neuromuscular Group, Department of Neurology and Neurosurgery, Montreal Neurological Institute and Hospital, McGill University, Montreal, QC, Canada

³Department of Psychiatry, Division of Behavioral Medicine, Department of Neurology and CTNI, Columbia University Medical Centre, New York, NY, USA

⁴Welcome Trust Centre for Mitochondrial Research, Institute of Neuroscience, The Medical School, Newcastle University, Newcastle upon Tyne, UK

Key points

- Mitochondrial-derived vesicle (MDV) formation occurs under baseline conditions and is rapidly upregulated in response to stress-inducing conditions in H9c2 cardiac myoblasts.
- In mice formation of MDVs occurs readily in the heart under normal healthy conditions while mitophagy is comparatively less prevalent.
- In response to acute stress induced by doxorubicin, mitochondrial dysfunction develops in the heart, triggering MDV formation and mitophagy.
- MDV formation is thus active in the cardiac system, where it probably constitutes a baseline housekeeping mechanism and a first line of defence against stress.

Abstract The formation of mitochondrial-derived vesicles (MDVs), a process inherited from bacteria, has emerged as a potentially important mitochondrial quality control (QC) mechanism to selectively deliver damaged material to lysosomes for degradation. However, the existence of this mechanism in various cell types, and its physiological relevance, remains unknown. Our aim was to investigate the dynamics of MDV formation in the cardiac system *in vitro* and *in vivo*. Immunofluorescence in cell culture, quantitative transmission electron microscopy and electron tomography *in vivo* were used to study MDV production in the cardiac system. We show that in cardiac cells MDV production occurs at baseline, is commensurate with the dependence of cells on oxidative metabolism, is more frequent than mitophagy and is up-regulated on the time scale of minutes to hours in response to prototypical mitochondrial stressors (antimycin-A, xanthine/xanthine oxidase). We further show that MDV production is up-regulated together with mitophagy in response to doxorubicin-induced mitochondrial and cardiac dysfunction. Here we provide the first quantitative data demonstrating that MDV formation is a mitochondrial QC operating in the heart.

(Received 25 April 2016; accepted after revision 13 June 2016; first published online 17 June 2016)

Corresponding author Y. Burrelle: Interdisciplinary School of Health Sciences, Faculty of Health Sciences, University of Ottawa, 451 Smyth Road, Ottawa, Ontario, Canada, K1N 8M5. Email: yburrell2@uottawa.ca

Abbreviations CRC, calcium retention capacity; Doxo, doxorubicin; FBS, fetal bovine serum; MDV, mitochondrial-derived vesicle; OCR, oxygen consumption rate; OMM, outer mitochondrial membrane; PDH, pyruvate dehydrogenase; PINK1, PTEN-induced putative kinase 1; QC, quality control; TEM, transmission electron microscopy; TOM20, translocase of the outer membrane; X/XO, xanthine/xanthine oxidase.

Introduction

Eukaryotic cells have evolved sophisticated quality control (QC) mechanisms that ensure repair or replacement of damaged macromolecules and organelles. At the level of mitochondria, the sustained biochemical activity essential for cell function inevitably induces a wear and tear of structural and metabolic components. Mitochondrial QC mechanisms include the cytosolic ubiquitin–proteasome system, which degrades mitochondrial proteins at the surface of the outer membrane, as well as chaperones and proteases that ensure degradation of damaged intra-mitochondrial proteins (for reviews see Kim *et al.* 2007; McBride & Scorrano, 2013; Lemasters, 2014). In addition, whole mitochondria that have accumulated excessive damage can be degraded through mitophagy, a process in which damaged organelles are specifically sequestered in double-membrane autophagosomes and delivered to lysosomes for degradation (Gottlieb & Carreira, 2010). Clearance of whole mitochondria through this process occurs on the scale of hours to days following a mitochondrial insult, and is regulated by multiple mechanisms including the PINK1/PARKIN and NIX/BNIP3 pathways, as well as cardiolipin-mediated mitophagy (Saito & Sadoshima, 2015).

In organs such as the heart, which has large mitochondrial biomass and nearly exclusive dependence on oxidative phosphorylation for energy supply (Stanley *et al.* 2005), mitophagy is suggested to play an important role in mounting an adequate response to stress (Gottlieb & Carreira, 2010; Delbridge *et al.* 2015). This view is supported by the observation that autophagy and mitophagy are upregulated in the heart following ischaemia–reperfusion (I-R) and sepsis, and by studies in mouse models showing that genetic inactivation of PARKIN attenuates stress-induced mitophagy, resulting in impaired recovery of mitochondrial and cardiac function (Kanamori *et al.* 2011a,b; Hoshino *et al.* 2012; Piquereau *et al.* 2013). However, uncertainty exists regarding the precise role of mitophagy on baseline mitochondrial housekeeping, in part because germline and inducible cardiac-specific deletion of PARKIN causes little (Piquereau *et al.* 2013) or no (Kubli *et al.* 2013; Song *et al.* 2015) mitochondrial dysfunction, and no detectable pathological phenotype at baseline.

In addition to mitophagy, recent studies in cellular models have uncovered a novel mitochondrial QC pathway, conserved from bacteria, in which mitochondria release small, mitochondrial-derived vesicles (MDVs) from their membranes to deliver specific mitochondrial contents to the late endosome/multivesicular bodies (Soubannier *et al.* 2012). MDVs are defined by at least three distinct criteria: independence on the core fission GTPase Drp1, the incorporation of selected mitochondrial cargo, and a diameter of 70–150 nm as observed by electron

microscopy. *In vitro* budding assays using bovine heart mitochondria have shown that MDVs are enriched with oxidized cargo, consistent with their role in maintaining mitochondrial health. While the mechanisms of cargo incorporation are unclear, evidence suggests vesicles can form exclusively from the outer membrane, or can be derived from both outer and inner membranes, carrying selected matrix content as well (Neuspiel *et al.* 2008; Soubannier *et al.* 2012a,b; McLelland *et al.* 2014; Sugiura *et al.* 2014). *In vitro* production of these populations of MDVs occurs not only under baseline conditions, but also rapidly (minutes to hours) in response to mitochondrial stress (McLelland *et al.* 2014). Moreover, MDVs form prior to mitochondrial depolarization (Soubannier *et al.* 2012a,b), suggesting that MDV formation represents an essential housekeeping mechanism and a first line of defence against mitochondrial stress. Interestingly, formation and transport of some double membrane MDVs enriched with matrix cargos was recently shown to require PINK1/PARKIN, indicating some level of interaction between MDV formation and mitophagy (McLelland *et al.* 2014).

Although the data gathered thus far suggest that MDV production is a potentially important mitochondrial QC mechanism, further studies are required to establish its physiological implication in various cell types and, most importantly, in intact organs *in vivo*. In the present study we used a combination of *in vitro* experiments in cardiac cells and quantitative morphological electron microscopy *in vivo* to test the hypothesis that MDV production is a physiological mechanism in the heart. We reveal for the first time that MDV production occurs in cardiac cells under normal baseline conditions, and can be up-regulated in response to relevant physiopathological stresses. These results have important implications for our understanding of mitochondrial QC in mammalian organs.

Methods

Ethical approval

All animal experiments were approved by the Université de Montréal animal ethics committee and performed in accordance with the guidelines of the Canadian Council of Animal Care.

Cell culture

H9c2 (2-1) myoblasts were purchased from ATCC (Manassas, VA, USA). Cells were initially cultured in high glucose DMEM (319-020-CL; Wisent Inc., Saint-Jean-Baptiste, QC, Canada) supplemented with sodium pyruvate (1 mmol l⁻¹, 600-110-EL; Wisent), penicillin/streptomycin (450-201-EL; Wisent) and 10%

fetal bovine serum (FBS, 37°C, 5% CO₂). To force cultured cells to rely on mitochondrial oxidative phosphorylation, glucose was replaced with galactose as the major energy substrate. For this, cells were cultured in glucose-free DMEM (319-060-CL; Wisent), supplemented with galactose (10 mmol l⁻¹), sodium pyruvate (1 mmol l⁻¹, 600-110-EL; Wisent), HEPES (10 mmol l⁻¹, 330-050-EL; Wisent), 1× penicillin/streptomycin (100 IU/100 µg ml⁻¹, 450-201-EL; Wisent) and 10% FBS. Cells were maintained in galactose media for 1 week prior to experiments.

Cell differentiation and treatments

H9c2 cells were differentiated into cardiomyocyte-like cells as previously described (Branco *et al.* 2012). Cells were plated in T75 flasks at a density of 35 000 cells ml⁻¹ in DMEM supplemented with galactose and allowed to sediment and adhere. After 24 h, FBS was reduced to 1% and the media supplemented with 10 nmol l⁻¹ retinoic acid (R2625; Sigma, St Louis, MO, USA) for six consecutive days (total DMSO added < 0.1%). At day 6, cells were plated at a density of 40 000 cells ml⁻¹ for further experiments. Cell treatments are indicated in the respective figures, as appropriate, and were: antimycin-A (20 µM, 60 min), xanthine (X0626; Sigma)/xanthine oxidase (X1875; Sigma) (50 µM at 25 mU ml⁻¹ and 100 µM at 50 mU ml⁻¹, 60 min), or doxorubicin (25 µM, D1515; Sigma, 30 min to 24 h). For each experimental condition appropriate time-matched controls were performed. All treatments were performed in 24-well plates with cells adherent to coverslips. Each 24-well included at least two time-matched control wells according to the experimental protocol.

Immunofluorescence

Immunofluorescence was performed as previously described (McLelland *et al.* 2014) with all solutions made in PBS (in mM: 136 NaCl, 2.6 KCl, 10 Na₂HPO₄, 1.8 KH₂PO₄, pH 7.4). Briefly, at the end of the treatments, cells were first fixed at 37°C in 5% paraformaldehyde, then quenched in NH₄Cl (50 mM), and permeabilized with 0.25% Triton-X. Cells were then blocked with 10% FBS for 1 h prior to primary antibody incubation (5% FBS, 1 h) and subsequent incubation with secondary antibody (5% FBS, 1 h, in the dark). The coverslips were then mounted on glass slides using ProLong Gold without and with DAPI, depending on the experiment (P36934 and P36935, respectively; Life Technologies, Carlsbad, CA, USA).

Confocal microscopy and vesicle quantification

Slides were imaged by confocal microscopy using a 100×, 1.4 NA objective on an LSM 510 Meta confocal microscope (Zeiss, Oberkochen, Germany). Excitation/emission

wavelengths were 561/640 nm for pyruvate dehydrogenase (PDH) and 488/520 nm for translocase of the outer membrane (TOM20). Acquired images were analysed using ImageJ (NIH, Bethesda, MD, USA). Vesicles were identified visually, based on apparent size and cargo selectivity (PDH positive or TOM20 positive, but not both) after application of a co-localization mask to discriminate them from mitochondria (which are positive for PDH and TOM20). Apparent vesicle size was ~300 nm, which represents an estimated actual size of ~50 nm considering the lateral resolution limit of confocal microscopy (Neupane *et al.* 2015). For the analysis, overlay TIF images were opened on ImageJ, colour channels were split, and the co-localization mask plugin was applied using only the green and red channels (ratio: 50%, Threshold 1 and 2: 50, Display value: 255). After this transformation, the mitochondrial network or any small mitochondria containing both PDH and TOM20 appeared white and were visually excluded from the analysis. On the resulting image the colour balance was then adjusted in each channel to a minimum below signal (30–60 to eliminate background) and maximum of 121 to enhance contrast. The resulting image was used to visually identify circular structures (>9 pixels²) positive for either PDH or TOM20 as previously described (McLelland *et al.* 2014). Data represent the average of 10–20 cells per experiment and at least three independent experiments, unless otherwise described in the figure legend. Quantitative analysis of mitochondrial morphology was conducted on the same cells in which MDV formation was quantified using the morphometric analysis application of the ImageJ software (W. S. Rasband, NIH, imagej.nih.gov/ij/, 1997–2012). Images of the mitochondrial network were first denoised with a median filter, followed by a top hat filter, to enhance the separation of mitochondria from the background (Koopman *et al.* 2006; Willems *et al.* 2009). Images were then binarized to create a mask, and submitted to particle analysis for acquiring form factor (FF = perimeter²/4π × area), aspect ratio (AR = long axis/short axis) and roundness (4 × [area]/π × [major axis²]) values. Form factor, aspect ratio and roundness were used as indicators of mitochondrial morphology: form factor – evaluation of mitochondrial complexity (the higher the form factor the higher the mitochondrial complexity, indicating a branched network); aspect ratio – evaluation of mitochondria elongation (1 being a perfect line); roundness – measurement of proximity to circularity (roundness is an indicator of mitochondrial network fragmentation and mitochondrial damage).

Measurement of oxygen consumption rates

Oxygen consumption rates (OCRs) were measured in H9c2 myoblasts using an XF24 Seahorse extracellular flux analyser (Seahorse Bioscience, North Billerica, MA

USA). Thirty thousand cells were plated in XF24 well plates in basal XF media supplemented with galactose (10 mM), sodium pyruvate (1 mM) and 2 mM glutaMax. Baseline OCR was recorded for 30 min following which 25 μM doxorubicin or its vehicle was injected. Baseline measurements were pursued for an additional 30 min, followed by the sequential addition of oligomycin (1 μM), CCCP (1 μM) and antimycin-A (1 μM). ATP-linked OCR was calculated as the difference between baseline and oligomycin-inhibited OCR. Maximal uncoupled respiration was derived from the maximal OCR reached 30 min after injection of CCCP. Proton leak-driven respiration was calculated as the difference between oligomycin-inhibited OCR and residual OCR measured after complete inhibition of the electron transport chain flux with antimycin-A. Wells were visually inspected before and after each experiment to ensure that no cells had detached during the assay. Values are reported in $\text{pmol O}_2 \text{ min}^{-1} 30,000 \text{ cells}$.

Animal experiments

Adult C57/BL6 mice (8–12 weeks, Charles River, Wilmington, MA, USA) were injected i.p. with doxorubicin (in PBS, 15 mg kg^{-1}) or with PBS (vehicle). Injections were made at 0 and 48 h. Five days following the second injection animals were anaesthetized with inhaled isoflurane (2%) and used for echocardiography, or killed by exsanguination and the hearts used for analysis of mitochondrial function in permeabilized cardiac fibre preparations, or electron microscopy.

Echocardiography

Echocardiography was performed as previously described (Aries *et al.* 2004; Marchesi *et al.* 2011). Briefly, mice were anaesthetized with 2% isoflurane (1 $\text{l min}^{-1} \text{ O}_2$) and their chest shaved. Mice were then placed on their back on a warming pad and the ratio of isoflurane/ O_2 was adjusted to achieve heart rate values between 500 and 550 bpm under light isoflurane. Echocardiography was performed using a Visual Sonic VEVO 770 ultrasound machine and an RMV 707B High Frame Rate Scanhead with a centre frequency of 30 MHz (VisualSonics Inc., Toronto, ON, Canada).

Permeabilized cardiac fibres

Mitochondrial functional assays in permeabilized muscle fibres. Left ventricle free walls were used for dissection and permeabilization of fibre bundles with saponin, as described previously (Piquereau *et al.* 2013). Some permeabilized fibres were incubated in a high KCl medium to render ghost fibres. Both permeabilized and ghost fibres were kept on ice until use. Mitochondrial functional parameters were measured in duplicate for

each biological replicate with a minimum of six biological replicates utilized per group. All mitochondrial functional parameters were expressed relative to dry fibre weight.

Mitochondrial respiration. Mitochondrial respiration was measured in permeabilized cardiac fibres [$< 2 \text{ mg}$ wet weight (Picard *et al.* 2008; Piquereau *et al.* 2013)] at 23°C, with constant stirring, in a respiration buffer [in mM: 2.77 CaCl₂ EGTA, 7.23 K EGTA (100 nM free Ca²⁺), 6.56 MgCl₂ (1 mM free Mg²⁺), 20 taurine, 0.5 DTT, 50 potassium methane sulfonate (160 mM ionic strength), 20 imidazole, pH 7.1]. Oxygen consumption rate ($\text{nmol O}_2 \text{ min}^{-1}$) was determined using the following sequence: complex I substrates glutamate–malate (5:2.5 mM); ADP (2 mM); the complex I blocker amytal (2 mM); the complex II substrate succinate (5 mM); the complex III blocker antimycin-A (8 μM); and the complex IV substrates *N,N,N'*-tetramethyl-*p*-phenylenediamine dihydrochloride (TMPD)–ascorbate (0.9:9 mM).

Mitochondrial H₂O₂ release. Mitochondrial H₂O₂ release was measured in permeabilized fibres incubated in a buffer (containing in mM: 110 K-MES, 35 KCl, 1 EGTA, 5 K₂HPO₄, 3 MgCl₂·6H₂O and 0.5 mg ml^{-1} BSA) with 1.2 U ml^{-1} horseradish peroxidase and the fluorescent probe Amplex red (20 μM : excitation–emission: 563 to 587 nm) at pH 7.3, 37°C (Ascah *et al.* 2011). Baseline fluorescence readings were taken prior to the addition of the following compounds: glutamate (5 mM), succinate (5 mM), ADP (10 mM) and antimycin-A (8 μM). Rates of H₂O₂ production were calculated as change in fluorescence per minute after subtraction of baseline.

Calcium retention capacity. Calcium retention capacity (CRC) was measured in ghost fibres in CRC buffer (in mM: 250 sucrose, 10 MOPS, 0.005 EGTA, 10 Pi-Tris, pH 7.3) supplemented with glutamate–malate (5:2.5 mM), 0.5 nM oligomycin and Ca-Green 5N (excitation–emission: 505 to 535 nm) as per Piquereau *et al.* (2013). Following the addition of fibres and respiratory substrates, a single pulse of 20 nmol of Ca²⁺ was added. CRC was defined as the total amount of Ca²⁺ accumulated by mitochondria prior to permeability transition pore (PTP) opening-induced Ca²⁺ release. Relative Ca²⁺ uptake was calculated as the difference between maximal Ca-Green fluorescence after calcium pulse addition and fluorescence level at the moment of PTP opening.

Enzyme activity

Activities of complex I (CI, NADH-CoQ reductase), complex II (CII, succinate dehydrogenase), complex I+III (CI+III, NADH-CoQ reductase + CoQ:cytochrome c reductase), complex IV (CIV, cytochrome oxidase

complex) and citrate synthase (CS) were measured spectrophotometrically in whole heart lysates with a plate reader using standard coupled enzyme assays as previously described (Marcil *et al.* 2006) with minor modifications (de Wit *et al.* 2008). Activities are expressed relative to control levels.

Transmission electron microscopy

Transmission electron microscopy (TEM) for morphological analysis or immunogold labelling was performed at the Facility for Electron Microscopy Research, McGill University, according to standard operating procedures. For morphological TEM, hearts from PBS- and doxorubicin-treated mice were fixed in 2.5% glutaraldehyde (Sigma) in phosphate buffer overnight at 4 °C. After sample preparation, 90–100 nm thick sections were mounted onto a 200 mesh copper grid (Electron Microscopy Sciences, Hatfield, PA, USA) and imaged with an FEI Tecnai 12 120 kV transmission electron microscope equipped with an AMT XR80C 8 megapixel CCD camera.

Immunogold labelling

Immunogold co-labelling of TOM20 and PDH was performed in heart slices from control and doxorubicin-treated animals using pre- and post-embedding methods. For pre-embedding, longitudinal left ventricular free-wall sections ~1 mm thick were fixed in 5% paraformaldehyde for 30 min at 37 °C. After blocking with 10% FBS in PBS, the sections were incubated overnight with primary antibodies (1:50–1:200 anti-PDH and anti-TOM20, 4°C). Following thorough washing with 5% FBS, the sections were incubated overnight (4°C) with gold-bound secondary antibodies. At the end of secondary antibody incubation the sections were thoroughly washed in PBS (6 × 10 min) and fixed in 2.5% glutaraldehyde in PBS for 15 min and processed as described above (see TEM section). For post-embedding immunolabelling, samples were fixed in a mixture of 4% paraformaldehyde and 0.5% glutaraldehyde for 4 h at 4°C. Samples underwent either the Tokuyasu method for cryo-immunolabelling (Tokuyasu, 1973) or LR White immunogold labelling. Primary antibody dilutions ranged between 1:2 and 1:5 with constant secondary antibody dilution of 1:20.

Quantification of MDV budding events by morphological TEM

For quantification of MDV in the heart, TEM images were acquired consecutively at a magnification of 9300× so as to image full cardiomyocytes. Images were manually screened by two independent raters to identify MDV budding events using the following criteria: (1) vesicular

structures had to have a diameter of 50–200 nm, (2) their membrane had to be contiguous to the mitochondrial membrane and of comparable electron density, (3) the electron density of the MDV had to be lower than that of the mitochondrial matrix for single membrane MDVs, and similar or higher for double membrane MDVs. For each cardiomyocyte, the average number of MDV per mm² was calculated. This analysis was performed in cardiomyocytes taken from randomly selected heart regions in 2–3 mice per experimental group. A total of 213 and 153 fields of view were analysed in control and doxorubicin-treated groups, respectively.

Electron tomography

For tomography, approximately 150–300 μm thick sections were imaged by dual axis image tilt series from –60 to +60 deg in 1.5 deg increments on a FEI Tecnai 12 microscope equipped with a Gatan US-1000 camera at 6500–12,000× magnification using SerialEM (Mastronarde, 2005). The etomo software package (Kremer *et al.* 1996) was used to reconstruct tomographic volumes from tilt series. From tomograms, three-dimensional reconstructions and video animations were generated using 3Dmod (IMOD 4.7, Boulder Laboratory for 3-D Electron Microscopy of Cells, CO, USA) and Image J (NIH, version 1.47v).

Statistical analysis

Unless indicated, data are presented as mean ± SEM. Unpaired Student's *t* test or a one-way ANOVA followed by Dunnett's or Bonferroni multiple comparison *post hoc* analysis was used to determine significant differences between two or among multiple groups, respectively. Statistically significant differences were considered at *P* < 0.05. All analyses were performed on Prism 6.0 for Mac OS-X.

Results

MDV formation in H9c2 cells occurs at baseline and is enhanced by prototypical oxidative stress

Previous studies have shown that in non-cardiac cells lines made reliant on mitochondrial metabolism (with galactose as primary energy substrate), induction of prototypical oxidative stress, by either complex III inhibition or exposure to xanthine/xanthine oxidase (X/XO) as a source of H₂O₂, stimulates the rapid production of MDVs destined for lysosomal degradation. The produced MDVs can be identified by their apparent size (300–600 nm by light microscopy) and more importantly their selective and high enrichment for markers of the matrix (e.g. PDH⁺/TOM20⁻; hereafter

PDH⁺) or the outer mitochondrial membrane (e.g. TOM20⁺/PDH⁻, hereafter TOM20⁺) (Neuspiel *et al.* 2008; Braschi *et al.* 2010; Soubannier *et al.* 2012a,b; McLelland *et al.* 2014).

To determine if a similar response occurred in a cardiac cell line model, PDH⁺ and TOM20⁺ MDVs were quantified in H9c2 myoblasts cultured in the presence of galactose at baseline and following short-term exposure to prototypical mitochondrial stresses. TOM20⁺ and PDH⁺ vesicles were consistently observed under baseline conditions (Figs 1A, D, 2A, C), indicating that vesicle shedding continuously occurs in the absence of exogenous mitochondrial stress. When cells were exposed to antimycin-A, a robust increase in the production of TOM20⁺ vesicles was observed within 60 min (Fig. 1B, D), while PDH⁺ vesicles did not change significantly. Aspect ratio, roundness and form factor were chosen as shape descriptors to evaluate the effects of mitochondrial or cellular stress on mitochondrial network morphology. Antimycin-A treatment did not significantly affect mitochondrial morphology (Fig. 1E–G), as no changes in these shape descriptors were observed.

Cells were also acutely exposed (60 min) to increasing amounts of X/XO to generate a sustained and global production of H₂O₂. At the lowest concentration of X/XO (50 μM/25 mU ml⁻¹) used, the production of TOM20⁺ and PDH⁺ vesicles was significantly increased compared to baseline values (Fig. 2B, D). This was accompanied by a significant increase in the aspect ratio and lower roundness values compared to baseline, suggesting relative hyperfusion of the mitochondrial network (Fig. 2E–G). At the highest concentration of X/XO (100 μM/50 mU ml⁻¹), the production of PDH⁺ MDVs, but not TOM20⁺, was elevated in comparison to baseline (Fig. 2C, D). However, in this condition, mitochondrial fragmentation was evident, as indicated by lower aspect ratio and form factor values, and increased roundness (Fig. 2E–G).

Of note, in preliminary experiments MDV production was also examined in cells cultured in glucose-containing media. Although MDVs were clearly being produced under baseline conditions, stress-induced MDV production could not be elicited in a reproducible manner (results not shown) consistent with the notion that cellular dependence of OXPHOS facilitates stress-induced MDV formation (Soubannier *et al.* 2012a). For this reason, all subsequent *in vitro* experiments were performed with galactose-containing media.

To further validate these results, experiments were next performed in H9c2 cells undergoing cardiomyocyte-like differentiation. Differentiation of H9c2 cells by serum restriction in the presence of retinoic acid induced polynucleation, and an increase in mitochondrial content (Fig. 3A–D). Interestingly, under baseline conditions the number of TOM20⁺ and PDH⁺ vesicles was three-fold greater in differentiated *vs* non-differentiated cells

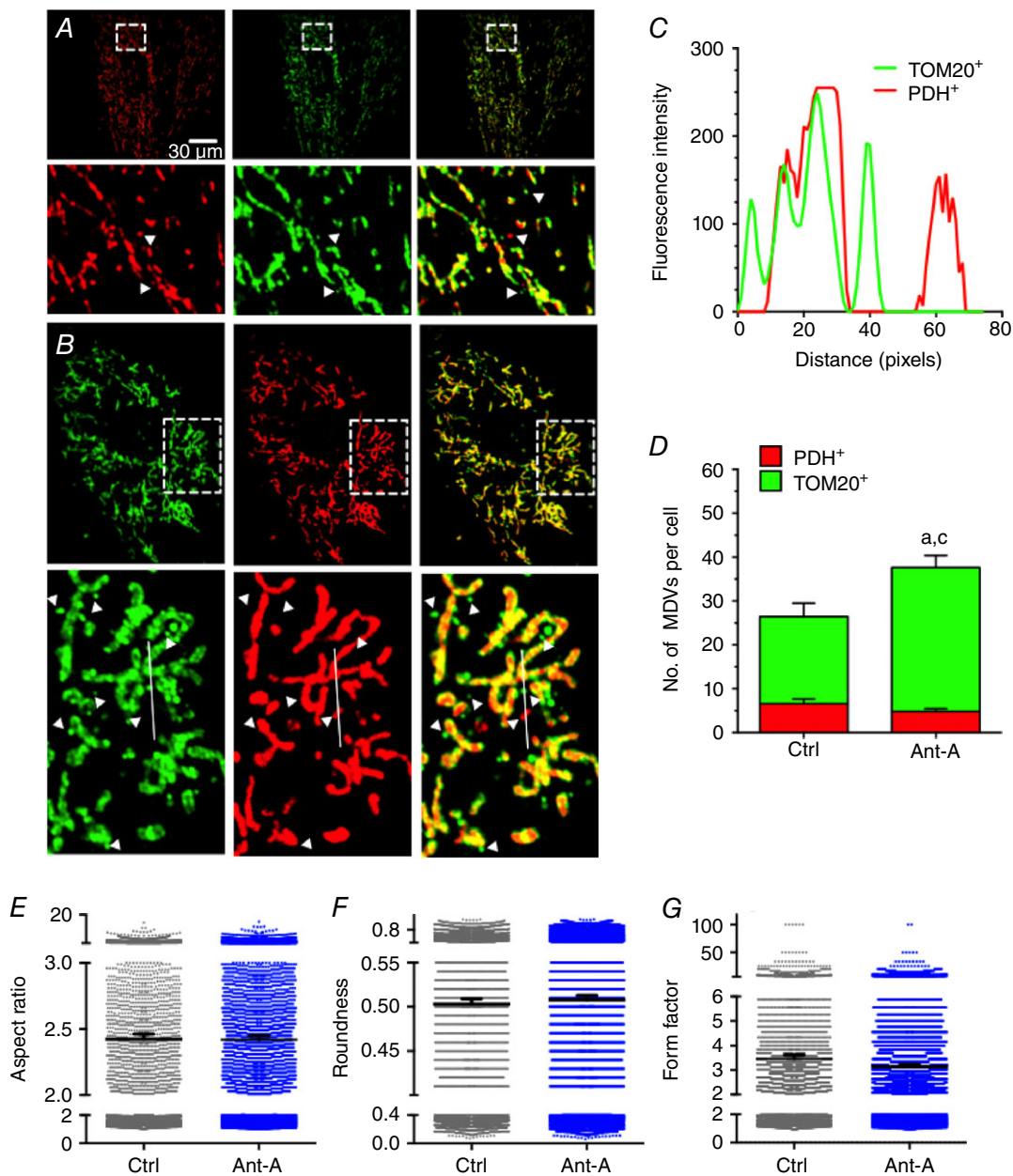
(Fig. 3E). However, despite the substantial increase in baseline MDV levels following differentiation, cells maintained their responsiveness to oxidative stress induced by X/XO (Fig. 3E), indicating that significant MDV formation occurs in differentiated cardiomyocyte-like cells, both at baseline and under conditions of oxidative stress.

Doxorubicin induces a rapid increase in MDV production in H9c2 cells that precedes mitochondrial network fragmentation

The observation of a functional MDV formation system in cardiac cells led us to investigate the impact of doxorubicin, a cardiotoxic anthracycline used for cancer treatment which is well known to induce mitochondrial injury. Acute exposure of H9c2 myoblasts to 25 μM doxorubicin for 30 min increased the production of TOM20⁺ and PDH⁺ vesicles (Fig. 4B, C). Respirometry experiments showed that between 30 and 120 min after exposure to doxorubicin, leak-driven, ATP-linked and maximal uncoupled oxygen consumption was not significantly altered compared to controls (Fig. 4D–G) indicating that enhanced MDV formation occurred prior to the accumulation of overt mitochondrial dysfunction. A detailed time course of MDV production was also performed over a 6 h period. As shown in Fig. 4, doxorubicin-induced MDV formation was maximal for both PDH⁺ and TOM20⁺ MDVs at 30 min, followed by a gradual decline until 6 h, without reaching control levels. Morphology analysis showed no evidence of mitochondrial network fragmentation at 30 min, when peak MDV production was achieved (Fig. 4M–O). Starting at 1 h, aspect ratio values declined and roundness increased but form factor remained mainly unchanged, indicating that mitochondrial network fragmentation was progressively beginning to occur. However, cell density and general morphology was unchanged during this period indicating the absence of significant cell death (Fig. 4I–L).

MDV formation occurs in the intact heart

To determine the physiological relevance of MDV production, we next focused on an *in vivo* mouse model. In a first set of experiments, acute inhibition of complex III by antimycin-A in isolated perfused mouse hearts was used to determine whether MDV formation, specifically budding events, could be visualized using TEM. Due to the relatively short duration of stress (10 min), overall cardiomyocyte morphology was preserved (Fig. 5A). Importantly, vesicular structures between 50 and 200 nm in diameter were identifiable at the surface of numerous mitochondria (Fig. 5Bi–iii). These vesicles were either single or double membraned, with the external membrane clearly contiguous with the outer mitochondrial membrane (OMM). Electron density of



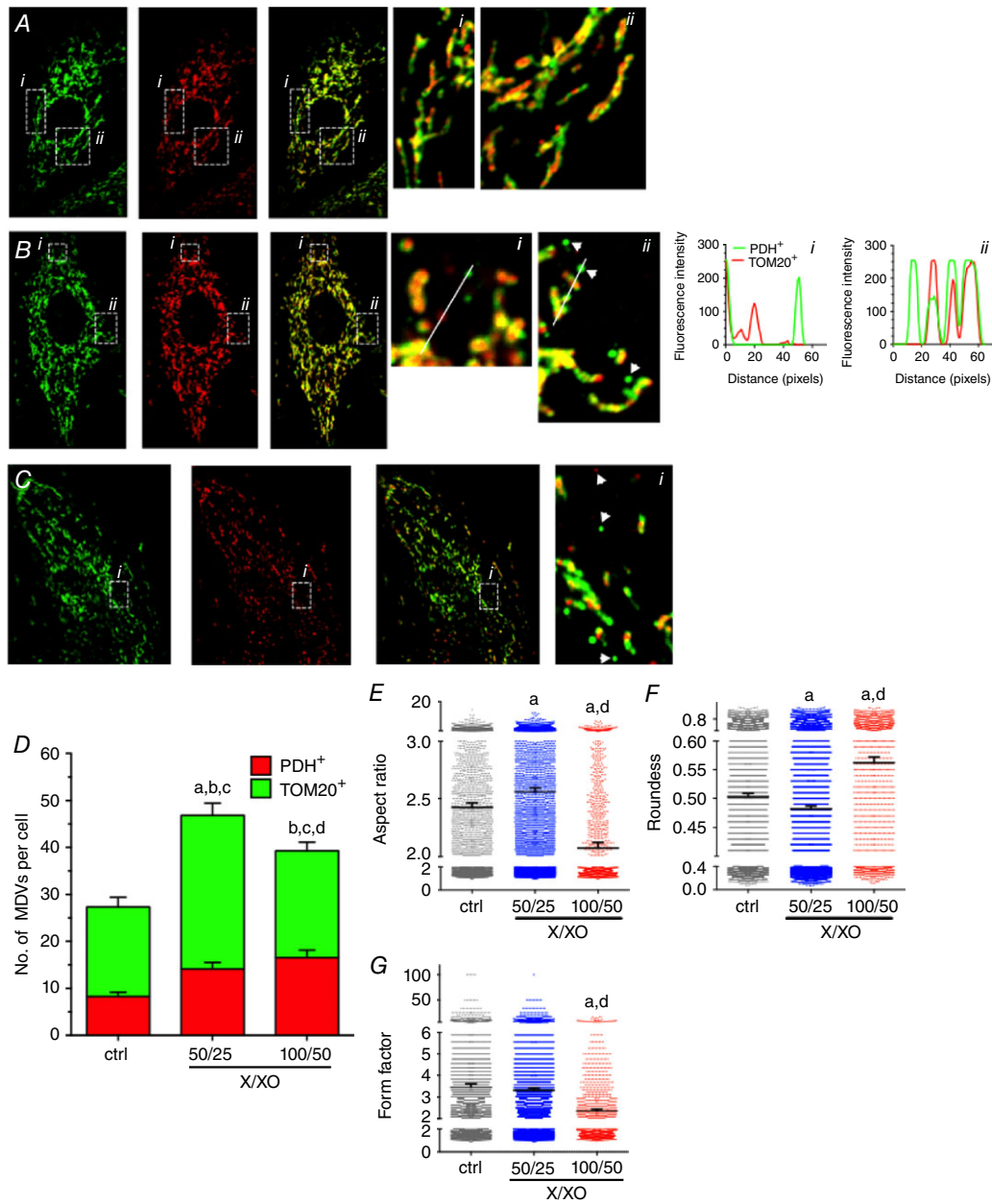


Figure 2. Increased TOM20⁺ and PDH⁺ MDV formation in response to H₂O₂ produced by the xanthine/xanthine oxidase system

A-C, H9c2 cardiac myoblasts cultured in galactose-containing media and treated with vehicle (A) or xanthine/xanthine oxidase (B: X/XO = 50/25 or C: 100/50 $\mu\text{M}/\text{mU ml}^{-1}$), for 60 min. Cells were immunolabelled for TOM20 (green) and PDH (red). Numbered panels on the right are magnifications of the boxed areas shown in the left panels. Fluorescence intensity plots along the illustrated lines are presented on the far right confirming that the structures identified as MDVs are indeed single labelled structures. D, quantification of TOM20⁺/PDH⁻ and PDH⁺/TOM20⁻ MDVs, as described in the Methods, in control and X/XO-treated cells at 60 min (three independent experiments per group, 10–12 random cells per experiment). Statistical comparison was made between X/XO and control and between the two X/XO concentrations using one-way ANOVA: a, $P < 0.01$ TOM20⁺/PDH⁻; b, $P < 0.01$ PDH⁺/TOM20⁻; c, $P < 0.01$ total MDVs; d, $P < 0.01$ TOM20⁺/PDH⁻ 50/25 vs 100/50. E–G, aspect ratio, roundness and form factor in control and X/XO-treated cells. Higher X/XO ratio resulted in increased fragmentation of the mitochondrial network (decreased form factor) and increased mitochondrial condensation (increased roundness) and decreased mitochondrial complexity (decreased aspect ratio). Values reported represent mean \pm 95% confidence interval for a minimum of 4000–6000 individual mitochondria. Mitochondrial morphology indicators were determined in the same cells used for MDV quantification. A, $P < 0.01$ X/XO vs control; d, $P < 0.01$ 50/25 vs 100/50 X/XO, one-way ANOVA. Images were selected to represent average quantification data.

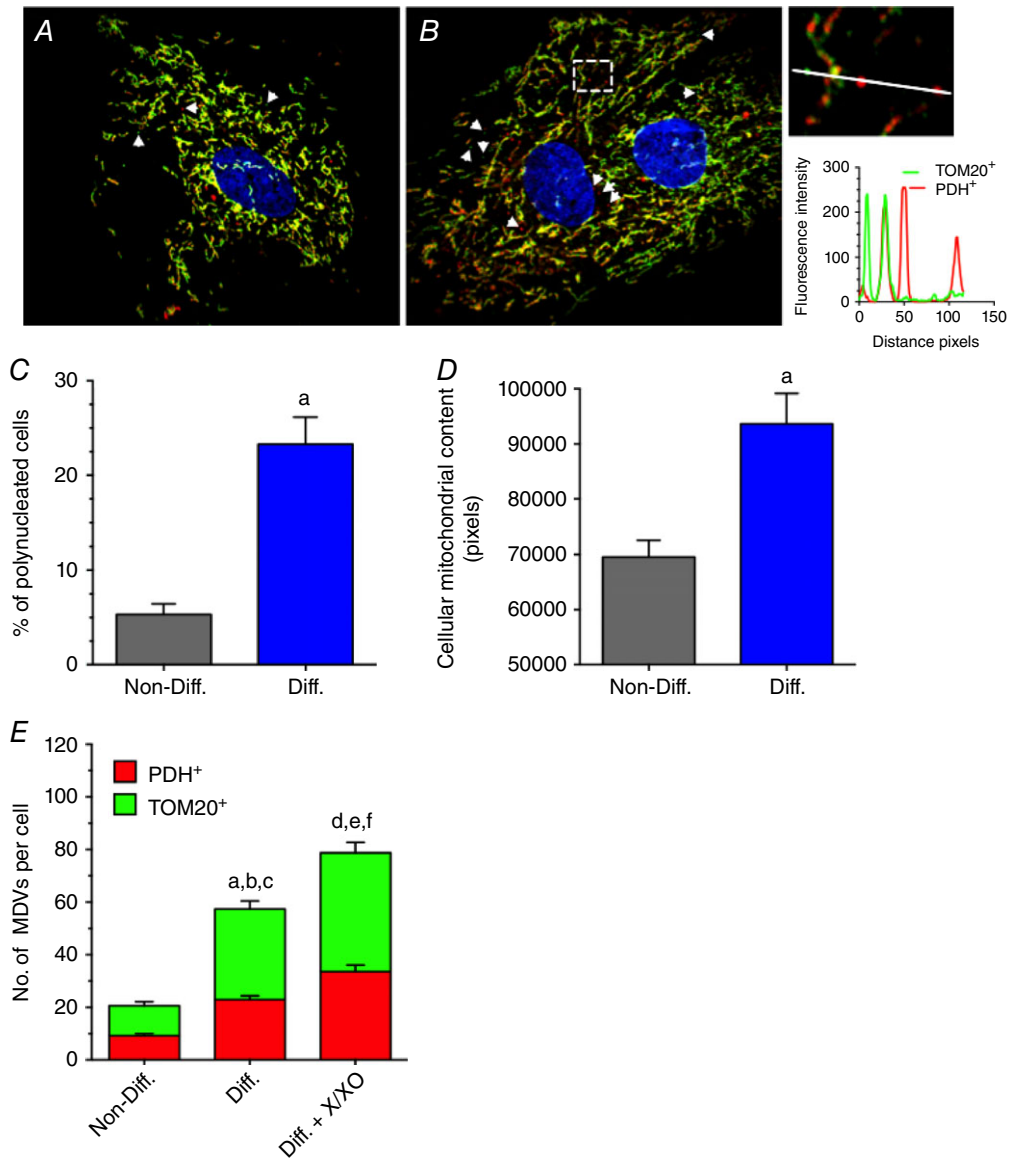


Figure 3. Effect of H9c2 cardiomyocyte-like differentiation on MDV formation triggered by H₂O₂
A and *B*, H9c2 cardiac myoblasts under control non-differentiated conditions (*A*) or following differentiation into ‘cardiomyocyte-like’ in the presence of 1% FBS and 10 nM retinoic acid (*B*). Cells were immunolabelled for TOM20 (green) and PDH (red), and nuclei were stained with DAPI. Arrowheads indicate TOM20⁺/PDH⁻ and PDH⁺/TOM20⁻ vesicles. The inset on the far right presents a magnification of the boxed region in *B*. A fluorescence intensity plot along the illustrated line is presented below. The line scan shows the presence of one TOM20⁺/PDH⁻ (green) and two PDH⁺/TOM20⁻ (red) vesicles near the doubly labelled mitochondrial network. *C*, percentage of polynucleated cells per field of view in non-differentiated and differentiated conditions as an indicator of cellular differentiation. *D*, cellular mitochondrial content measured as the cellular surface occupied by mitochondria in non-differentiated and differentiated conditions as another indicator of cellular differentiation; a, $P < 0.01$ differentiated vs. non-differentiated using unpaired *t* tests. *E*, quantification of TOM20⁺/PDH⁻ and PDH⁺/TOM20⁻ MDVs in non-differentiated and differentiated cells at baseline, and following exposure to X/XO for 60 min. Statistical comparison using one-way ANOVA was made between differentiated and non-differentiated (a, $P < 0.01$ TOM20⁺/PDH⁻; b, $P < 0.01$ PDH⁺/TOM20⁻; c, $P < 0.01$ total MDVs) and between differentiated and differentiated X/XO (d, $P < 0.01$ TOM20⁺/PDH⁻; e, $P < 0.01$ PDH⁺/TOM20⁻; f, $P < 0.01$ total MDVs). All values reported are mean \pm SEM of at least three independent experiments per group (10–12 random cells per experiment). Images were selected to represent average quantification data.

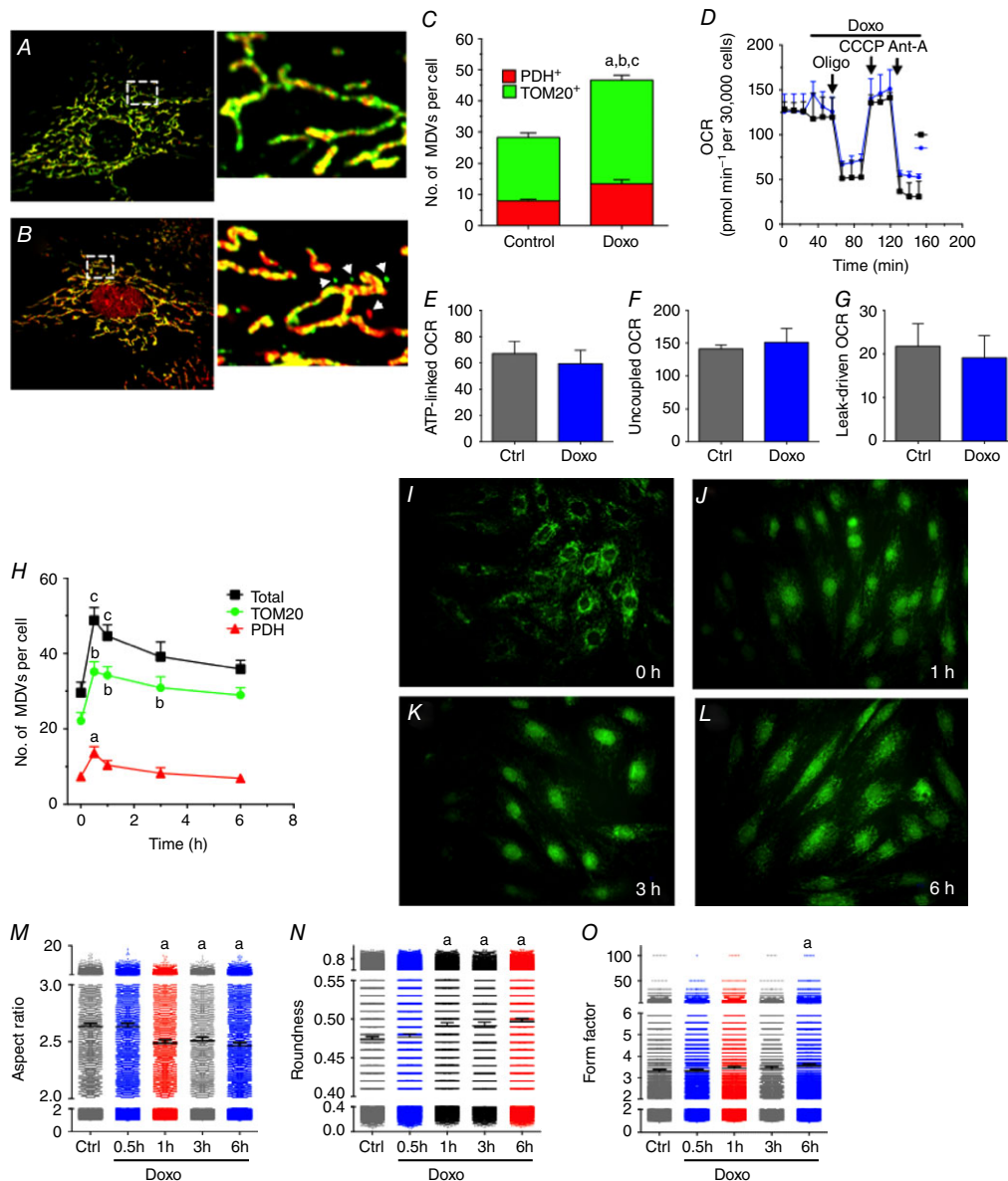


Figure 4. Acute doxorubicin treatment triggers rapid MDV production in H9c2 cells in the absence of mitochondrial dysfunction and mitochondrial network fragmentation

A and B, H9c2 cardiac myoblasts cultured in galactose-containing media and treated with vehicle (A) or 25 μM doxorubicin (B) for 30 min. As in the previous figures, cells were immunolabelled for TOM20 (green) and PDH (red). In treated cells, doxorubicin fluorescence is also visible in nuclei. Insets on the right represent magnifications of boxed regions represented in A and B. Arrowheads indicate TOM20⁺/PDH⁻ and PDH⁺/TOM20⁻ vesicles. C, quantification of TOM20⁺/PDH⁻ and PDH⁺/TOM20⁻ MDVs in control and doxorubicin-treated cells at 30 min as described in the Methods. Statistical comparison was made between doxorubicin and control using unpaired *t* tests: a, $P < 0.01$ TOM20⁺/PDH⁻; b, $P < 0.01$ PDH⁺/TOM20⁻; c, $P < 0.01$ total MDVs. D, oxygen consumption rate (OCR) profile in H9c2 cells exposed to vehicle or 25 μM doxorubicin added after recording baseline OCR. Where indicated, oligomycin (Oligo), CCCP and antimycin-A (Ant-A) was injected to derive key parameters of mitochondrial respiration such as ATP-linked, maximal CCCP-uncoupled, and leak-driven respiration computed from the OCR profiling tests (E–G, respectively). H, time course analysis of MDV formation in cells exposed to 25 μM doxorubicin. Statistical symbols are similar to C but a one-way ANOVA was used for the analysis. I–L, H9c2 myoblasts immunolabelled for TOM20 and imaged at low magnification (40 \times). Over the 6 h kinetics, no cell death was observed as evidenced by preserved cell density and general mitochondrial/cellular morphology. M–O, mitochondrial network morphology assessed as aspect ratio, roundness and form factor in control and doxorubicin-treated cells. Statistical symbols are similar to C but a one-way ANOVA was used for the analysis. All values reported are mean \pm SEM of at least three independent experiments per group (10–12 random cells per experiment). For mitochondrial morphology, data are reported as mean \pm 95% confidence interval for a minimum of 4000–6000 individual mitochondria. Images were selected to represent average quantification data.

the single membrane vesicles was generally low, relative to the mitochondrial matrix (Fig. 5*Biii*), while double membrane vesicles had an electron density that was similar or higher (Fig. 5*Bi, ii*). Vesicles were also clearly distinct from surrounding sarcoplasmic reticulum (SR) tubules

or from small mitochondria undergoing fission or fusion (Fig. 5*Bii*).

To clearly distinguish MDV formation from fusion/fission events and to obtain better spatial resolution, electron tomography was performed. Figure 5(*Ci–xii*)

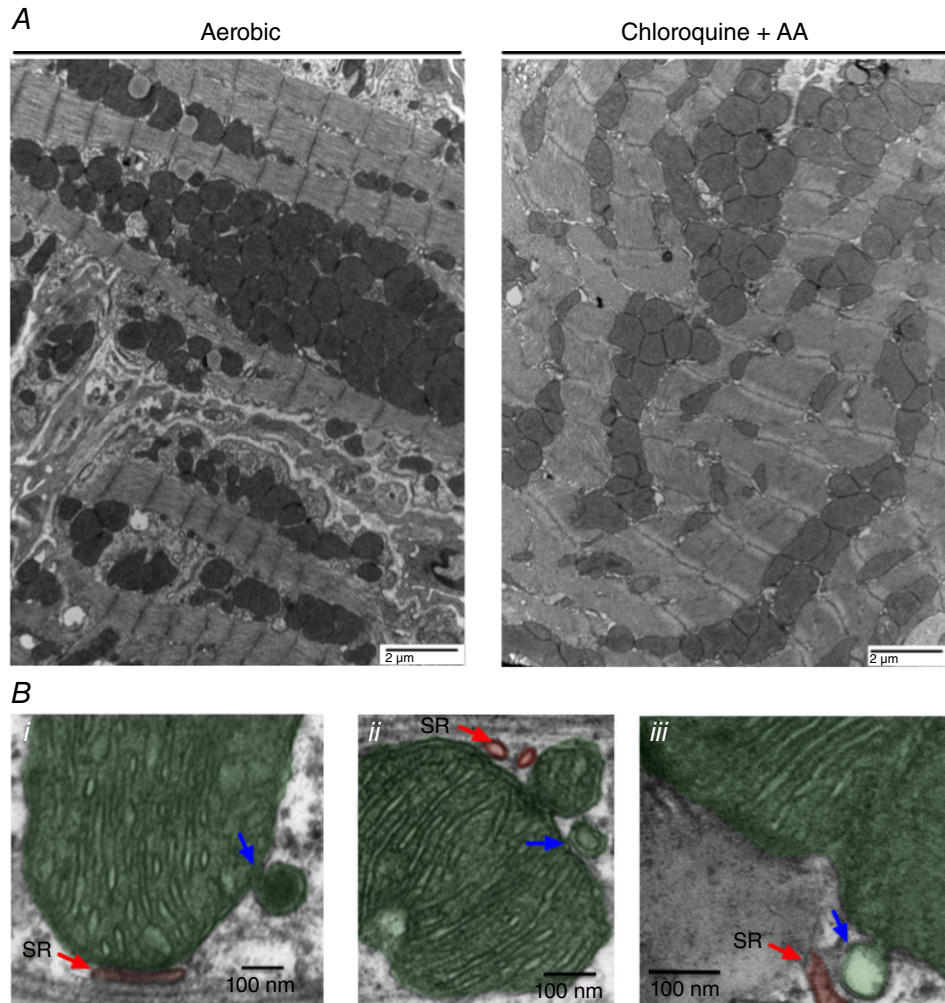


Figure 5. Identification and modelling of MDVs produced *in vivo* in the mouse heart

Identification of MDVs *in vivo* was performed in isolated hearts perfused for 30 min without or with chloroquine 30 μM /antimycin-A (40 μM during last 10 min). Following perfusion, heart sections were fixed in 2.5% glutaraldehyde and imaged by TEM. *A*, low-magnification images indicate good preservation of cardiomyocyte ultrastructure in hearts perfused with chloroquine/antimycin-A for a short time period. *B*, identification of MDV budding events in several higher magnification images. Single and double membrane MDVs (blue arrows) can be distinguished from sarcoplasmic reticulum tubules (shaded red in *Bi–iii*) or mitochondrial fission/fusion events (see small mitochondria in *Bii*). *C*, electron tomogram of distinct sections from a chloroquine/antimycin-A perfused heart. *Ci–iii* and *vii–ix* show serial z stack images of a mitochondrion presenting two MDV-like structures in the process of budding (black arrows). *Civ–vi* and *x–xii* show the same images but the remodelled areas are shaded in green, cyan or magenta for increased clarity. *D*, 3D reconstruction of the region presented in *C*. The arrows point to the MDV-like structures still budded to the mitochondria. One vesicle is ~ 60 nm in diameter and is composed solely of the OMM (green). The other vesicle, which is ~ 90 nm in diameter, is attached to the mitochondrial OMM on the lower portion of its height (green), while the upper portion is separated (magenta). This structure contains some inner membrane (yellow) but does not present the typical electron density of the matrix (*C*). A mitochondrion of about 350 nm in diameter in the process of fission or fusion is also visible in the reconstructed region. Part of its outer membrane is attached to the mother organelle (green), while the upper portion (cyan) is separated. Electron density of this small mitochondrion is typical of the mitochondrial matrix and comparable to that of the larger organelle.

shows serial z planes of two vesicular structures 60 and 90 nm in diameter budding from mitochondria. Three-dimensional reconstruction showed membrane contiguity between these structures and the OMM across several z planes. One was composed of a single layer of OMM, while the other contained some inner membrane and had an overall electron density that was much lower than the mitochondrial matrix. In addition, the reconstructed region included a small mitochondrion of approximately 300–400 nm diameter in the process of fission or fusion. This mitochondrion, in contrast to budding vesicles, contained an organized cristae arrangement and had an electron density that was typical of the mitochondrial matrix (Fig. 5D).

Doxorubicin-induced mitochondrial dysfunction triggers MDV production in mouse heart

To determine whether MDV production occurs *in vivo*, a commonly used model of acute doxorubicin cardiotoxicity was used in C57BL/6 mice (Diotte *et al.* 2009; Zhang *et al.* 2009; Kawaguchi *et al.* 2012; Hoshino *et al.* 2013). As shown in Table 1, doxorubicin-treated mice had a lower body weight, displayed early signs of cardiac remodelling, but had a preserved ejection fraction. Several signs of mitochondrial dysfunction were present including reduced activity of complex I, impaired baseline and ADP-stimulated respiration in the presence of substrates for complex I, II and IV, reduced

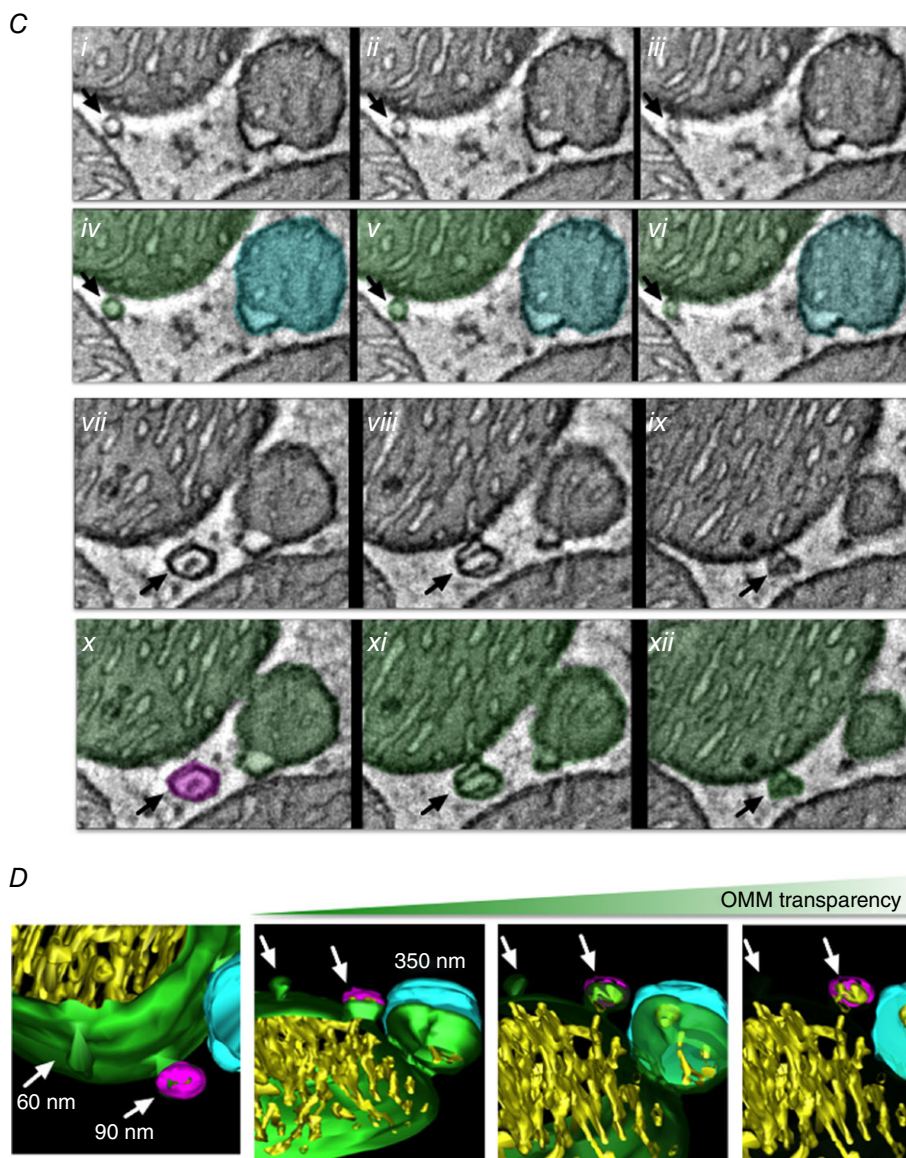


Figure 5. Continued

Table 1. Haemodynamic characterization by echocardiography of mouse hearts

	Vehicle	Doxorubicin	<i>n</i>	<i>P</i>
Age (weeks)	2.602 ± 0.061	2.724 ± 0.121	7	0.395
BW (g)	29.171 ± 0.898	23.486 ± 1.157	7	0.002
IVSd (mm)	0.781 ± 0.027	0.874 ± 0.049	7	0.126
LVIDd (mm)	3.912 ± 0.061	3.469 ± 0.184	7	0.042
LVPWd (mm)	0.827 ± 0.041	0.849 ± 0.061	7	0.774
IVSs (mm)	1.292 ± 0.043	1.289 ± 0.074	7	0.971
LVIDs (mm)	2.523 ± 0.096	2.179 ± 0.118	7	0.043
LVPWs (mm)	1.196 ± 0.069	1.239 ± 0.077	7	0.683
mm-mode RR	113.337 ± 1.013	114.513 ± 1.241	7	0.476
HR (bpm)	529.648 ± 4.770	524.328 ± 5.725	7	0.487
FS (%)	35.583 ± 1.765	36.766 ± 2.998	7	0.740
LV mass (mg)	114.775 ± 5.811	104.623 ± 9.114	7	0.366
LV mass index (mg g ⁻¹)	3.974 ± 0.267	4.502 ± 0.446	7	0.330
LV mass cor	91.820 ± 4.640	83.699 ± 7.296	7	0.366
Lvmass cor index	3.179 ± 0.220	3.602 ± 0.353	7	0.330
RWT	0.412 ± 0.012	0.506 ± 0.034	7	0.024
LVVd (μl)	66.542 ± 2.455	51.114 ± 6.323	7	0.042
LVVs (μl)	23.180 ± 2.208	16.322 ± 2.235	7	0.050
EF	65.444 ± 2.354	66.934 ± 3.924	7	0.750

BW, body weight; IVSd/s, intraventricular septum (diastole/systole); LVIDd/s, left ventricular inner diameter (diastole/systole); LVPWd/s, left ventricular posterior wall (diastole/systole); HR, heart rate; FS, fractional shortening; RWT, relative wall thickness; LVVd/s, left ventricular volume (diastole/systole); EF, ejection fraction.

Ca²⁺ retention capacity, and enhanced oxidative stress evidenced by greater H₂O₂ release and lower aconitase activity (Fig. 6A–E, respectively).

As acute doxorubicin treatment resulted in mitochondrial dysfunction, we sought to quantify MDV formation. In preliminary experiments, dual immunogold labelling of TOM20 and PDH was performed in pre- or post-embedded heart slices from control animals. Positively stained MDV-like vesicular structures could be identified in pre-embedded samples (Fig. 7Ai, ii). However, due to a combination of low antibody penetration in the cardiac tissue and low antigenicity, this method did not yield sufficient analysable data. Abundant labelling of mitochondria could be achieved using post-embedding, which improves antigen access. However, preservation of ultrastructure was dramatically reduced and insufficient to resolve small vesicular structures (Fig. 7Aiii, iv). For these reasons morphological TEM analysis was used for quantification of MDV budding events, by acquiring serial, high-magnification images (9300×) which were then stitched together to reconstitute entire cardiomyocytes from the left ventricular free wall (Fig. 7B). Systematic quantification of MDV budding events was performed by two independent raters in cardiomyocytes taken from vehicle and doxorubicin-treated mice. Spearman's rank coefficient (ρ) values of 0.74, $P < 0.0001$ (Fig. 7C), were obtained demonstrating good inter-rater reliability. Using this approach, mitochondrial vesicle budding was frequently observed in hearts from

control mice. Furthermore, in response to doxorubicin treatment the incidence of vesicle budding from mitochondria more than doubled, in comparison to control (Fig. 7D). The average diameter of budding vesicles was 79 ± 2 and 86 ± 2 nm in control and doxorubicin groups, respectively (Fig. 7E). In addition, the accumulation of small, MDV-like vesicles immediately surrounding mitochondria was significantly higher in hearts from doxorubicin-treated mice compared to controls (Fig. 8A, B). Quantification of autophagosomes containing mitochondria was also performed on the same samples. As shown in Fig. 8(F), autophagosomes containing mitochondria could only be found in hearts from doxorubicin-treated mice. However, the number of mitophagosomes was an order of magnitude lower than the number of MDV budding events.

Discussion

Throughout the last decade, mitochondrial function and QC have been the subject of increased research focus. Mitochondrial QC mechanisms, including MDV formation, may represent novel targets for modulation of mitochondrial function and cell survival, but remain to be solidly validated in several cell types and, more importantly, *in vivo*, under both physiological and pathological conditions. In this study, we provide novel evidence supporting a role for MDV formation in mitochondrial QC in the cardiac system.

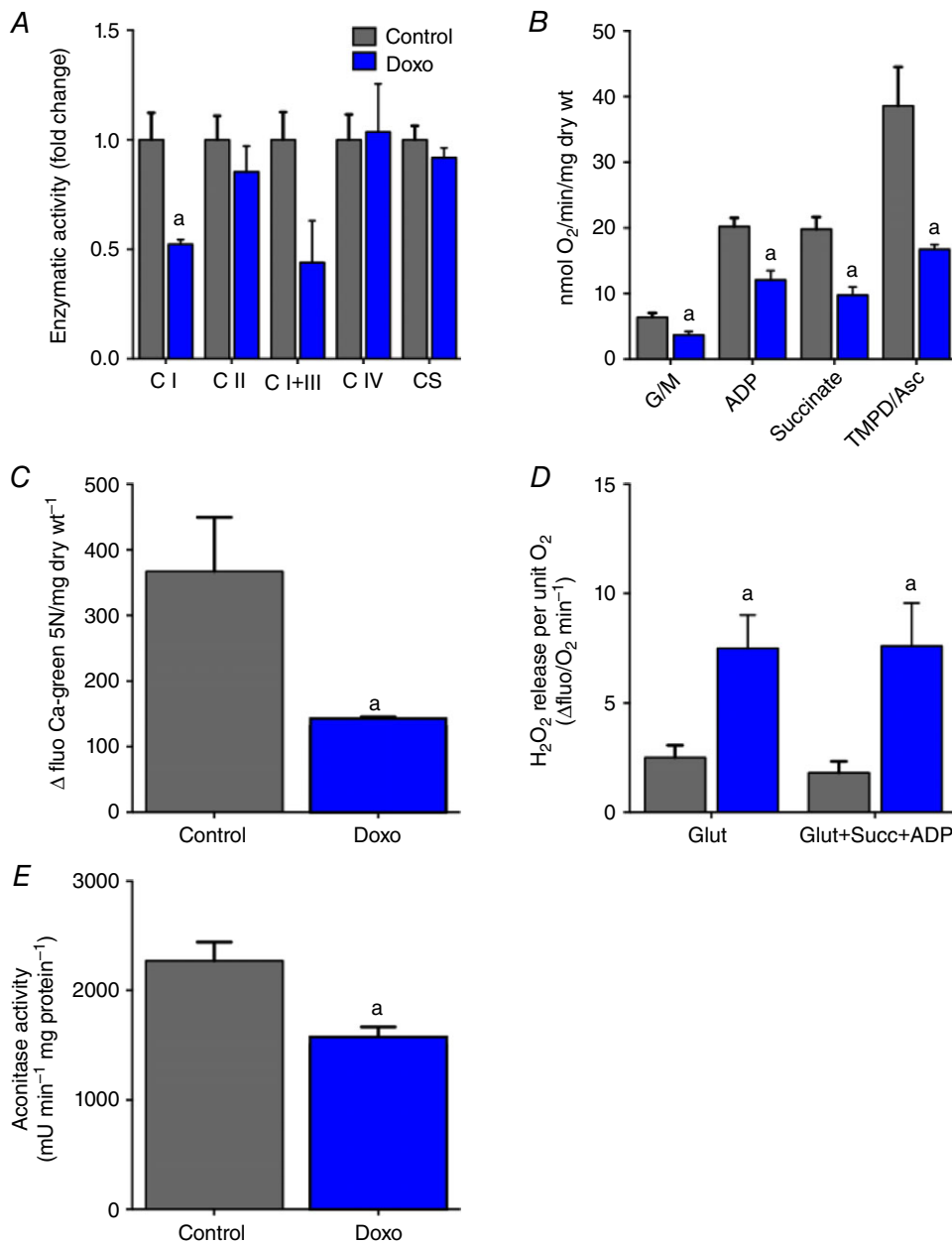


Figure 6. Effect of acute doxorubicin treatment on cardiac mitochondrial function

Mitochondrial function was characterized in mouse hearts 5 days after acute doxorubicin treatment as described in the Methods. *A*, enzymatic activity of complex I, II, I+III, IV and citrate synthase was measured in whole heart lysates. *B*, respiratory function measured in saponin-permeabilized cardiac fibre bundles. Respiration was measured following sequential addition of the CI substrates glutamate + malate (G/M), ADP, the C-II substrate succinate and the CIV substrate TMPD/ascorbate. *C*, Ca²⁺ retention capacity measured in permeabilized cardiac fibres using calcium green 5N. Reduced Ca²⁺ retention is indicative of premature opening of the PTP. *D*, net mitochondrial H₂O₂ release measured in permeabilized cardiac fibres under state 2 conditions in the presence of the CI substrate glutamate or under state 3 conditions in the presence of ADP and a combination of glutamate and succinate to provide a dual input of electrons at C-I and C-II. *E*, activity of the ROS-sensitive mitochondrial enzyme aconitase measured in whole heart lysates. Values represent the mean ± SEM for *n* = 4–8 mice per group. *A*, *P* < 0.05 vs. control; two-way ANOVA multiple comparisons for mitochondrial respiration and H₂O₂ release, and unpaired *t* test for enzymatic activity, calcium retention capacity and aconitase activity.

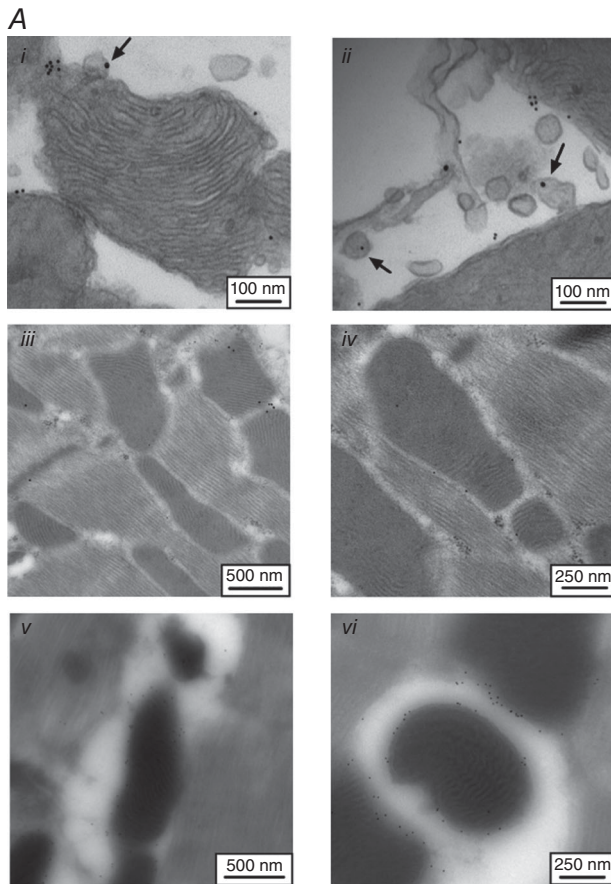


Figure 7. MDV formation is increased by acute doxorubicin treatment in the mouse heart

A, immunogold labelling of PDH and TOM20 in the heart. Hearts from control and doxorubicin-treated animals were subjected pre- and post-embedding immunogold labelling protocols. Pre-embedding (*i, ii*) provided higher image quality and high-specificity binding, but little labelling due to poor antibody penetration, and thus low yield of analysable images. Post-embedding (*iii–vi*) provides high-specificity binding with high sensitivity but very low structural resolution images for MDV identification. B, heart sections from control and doxorubicin-treated mice were fixed for TEM analysis. Successive images acquired at a magnification of 9300 \times were stitched together to reconstitute whole cardiomyocytes. Numbered (*i–iii*) insets represent magnifications of the boxed regions of the left panel. On the far right are representative examples of MDVs, budding from mitochondria, that were included in the quantification (shaded green). C, number of MDV budding events per field of view assessed by two independent raters. Each dot represents a single field of view ($n = 170$). Average \pm 95% confidence interval of the linear regression analysis is shown along with the Spearman rho (ρ) coefficient, which is indicative of inter-rater agreement level. D, quantification of MDV budding events in control and doxorubicin-treated mice reported as number of MDVs per mm² of cardiomyocyte surface area. E, major diameter of MDVs in control and doxorubicin-treated mice. Data were obtained from a total of 366 distinct fields of view reconstituting entire cardiomyocytes from 2–3 different mice per experimental group. Each dot represents the average value obtained in distinct cells selected randomly. a , $P < 0.05$ vs. control, unpaired t test. Images were selected to represent average quantification data.

Our *in vitro* experiments performed in H9c2 cells reveal important characteristics of the MDV production system in cardiac-like cells. We show that TOM20⁺ and PDH⁺ vesicles, the two types of MDVs recently suggested to be involved in the segregation and delivery of oxidized mitochondrial proteins to lysosomes (Soubannier *et al.* 2012a), are produced in cardioblasts under normal cell culture conditions, indicating that MDV formation is an active baseline process. Consistent with our initial observations (Soubannier *et al.* 2012a), MDV production is more readily observable when cardioblasts are made reliant on OXPHOS for energy production (i.e. in galactose-containing media), confirming that this process is commensurate with mitochondrial metabolic activity. In this regard, we also observed that baseline production of TOM20⁺ and PDH⁺ vesicles is substantially enhanced in cardioblasts undergoing differentiation. Although the mechanisms underlying this increase in expression have not yet been established, it is striking that it occurs at a time when cells are undergoing significant reprogramming towards oxidative metabolism. In H9c2 cells, this reprogramming not only implies an increase in mitochondrial content and function, but also significant changes in their molecular makeup, requiring an increase in both protein biosynthesis and elimination (Bisetto *et al.* 2013; Branco *et al.* 2015; Kuznetsov *et al.* 2015). Thus, increased MDV formation during cardioblast differentiation may reflect the increasing metabolic activity of mitochondria, and the subsequent need for degradation of specific subsets of proteins (Katajisto *et al.* 2015).

In addition to being produced under basal cell culture conditions, our data demonstrate that in cardiac-like cells MDV production is rapidly up-regulated over a time scale of minutes to hours following exposure to mitochondrial stressors. *In vitro* time course experiments in cells treated with doxorubicin showed that peak MDV production was achieved within 30 min, and remained elevated for 3–6 h, in the absence of bioenergetic impairments, and overt fragmentation of the mitochondrial network. Enhanced production of MDVs was also observed within 60 min of exposure to antimycin-A and X/XO. These data bare resemblance to time course studies performed in E2OS cells, where we found MDV production to be upregulated during the first 4 h of exposure to antimycin-A. In these studies, whole organelle mitophagy was also detected but only after 12–24 h (Chan *et al.* 2011; McLelland *et al.* 2014), which is consistent with previous measurements of mitophagy kinetics (Chan *et al.* 2011; McLelland *et al.* 2014). Together these data suggest that formation of MDVs may constitute a first line of defence to limit the accumulation of overt mitochondrial damage, which would otherwise result in the onset of whole organelle mitophagy (Sugiura *et al.* 2014), a process that is arguably more complex and costly for cells.

The molecular mechanisms governing MDV formation are currently unclear. Recent work showed that formation and transport of a subset of PDH⁺ vesicles was dependent on PINK1/PARKIN, indicating some degree of cross-talk with mitophagy (McLelland *et al.* 2014). However, because this represents only a fraction of MDVs being produced (e.g. ~20% of PDH⁺ vesicles), it is likely that additional players, such as members of the Rab protein family, or other vesicle-related proteins of uncharacterized function, may play a more central role (Sugiura *et al.* 2014).

Technical limitations regarding the specific monitoring of distinct QC mechanisms in intact organs under a variety of conditions pose a major challenge for assessing the physiological relevance of mitochondrial QC mechanisms.

In the present study, we provide extensive electron microscopy evidence demonstrating that MDV production represents a dynamic system in the heart *in vivo*. Using morphological TEM and electron tomography imaging techniques, we show that MDV budding occurs in cardiac mitochondria, and can be clearly distinguished from fission/fusion events. Quantitative analysis of MDV budding events confirms our *in vitro* observations, demonstrating that budding events are frequent in the normal heart under baseline conditions. Importantly, the number of MDV budding events increases significantly in response to acute doxorubicin-induced mitochondrial and cardiac dysfunction. Notably, the numbers we report probably underestimate the true amount of MDVs

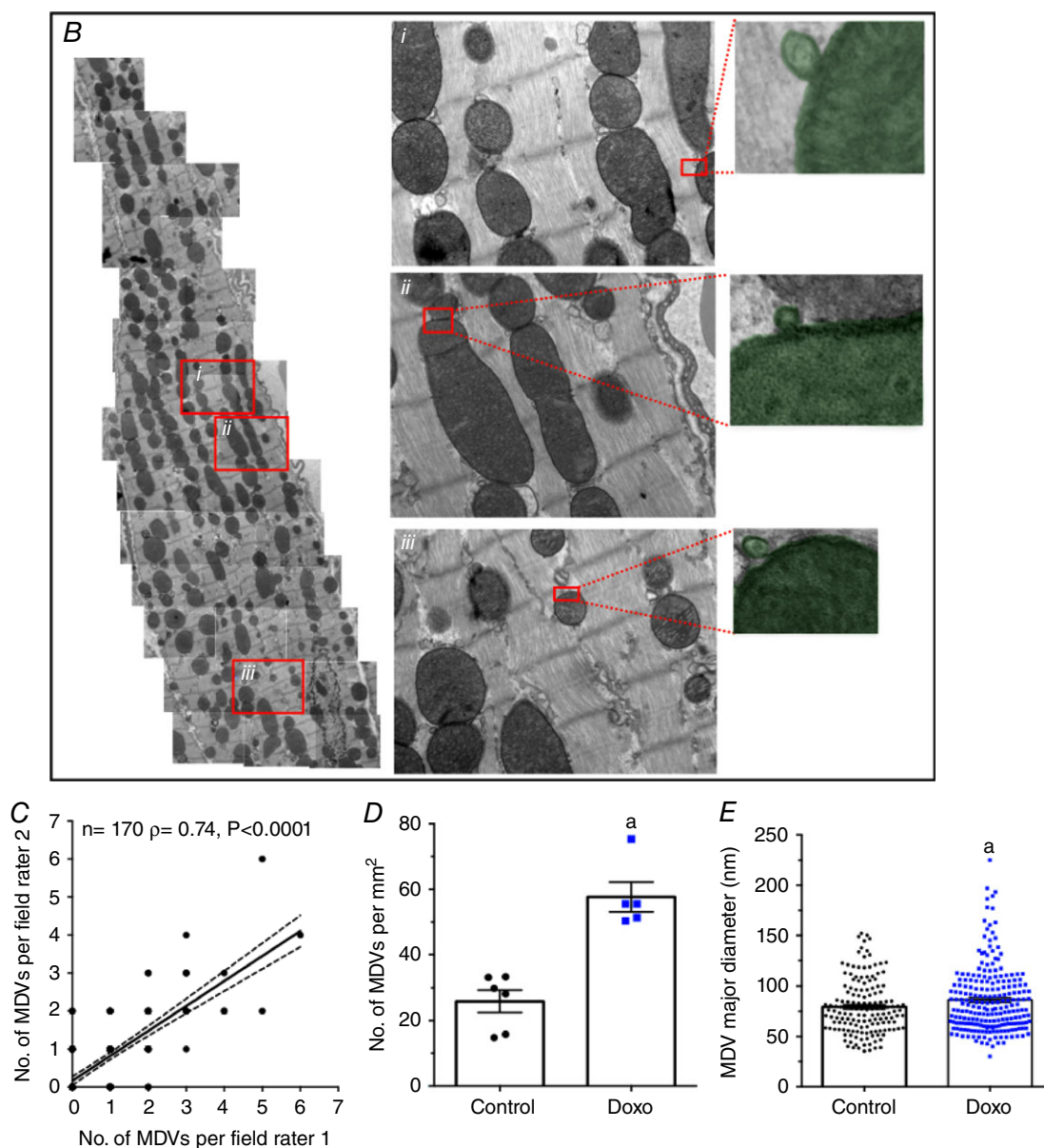


Figure 7. Continued

present in cardiomyocytes, as they only consider vesicles in the process of budding. This may be particularly true under stress conditions where the rate of MDV production increases significantly. In this regard, it is striking that, in the hearts of doxorubicin-treated animals, clusters of small vesicles resembling MDVs were frequently observed in the vicinity of numerous mitochondria. Development of specific markers for MDVs that circumvent the

current limitations of immunogold labelling would be required to confirm the origin of these peri-mitochondrial vesicles, and to obtain a precise quantification of MDV flux.

The role of mitophagy and its contribution to cardiac mitochondrial turnover under normal and pathological conditions remain unclear and somewhat controversial (Saito & Sadoshima, 2015; Wei *et al.* 2015). In the present

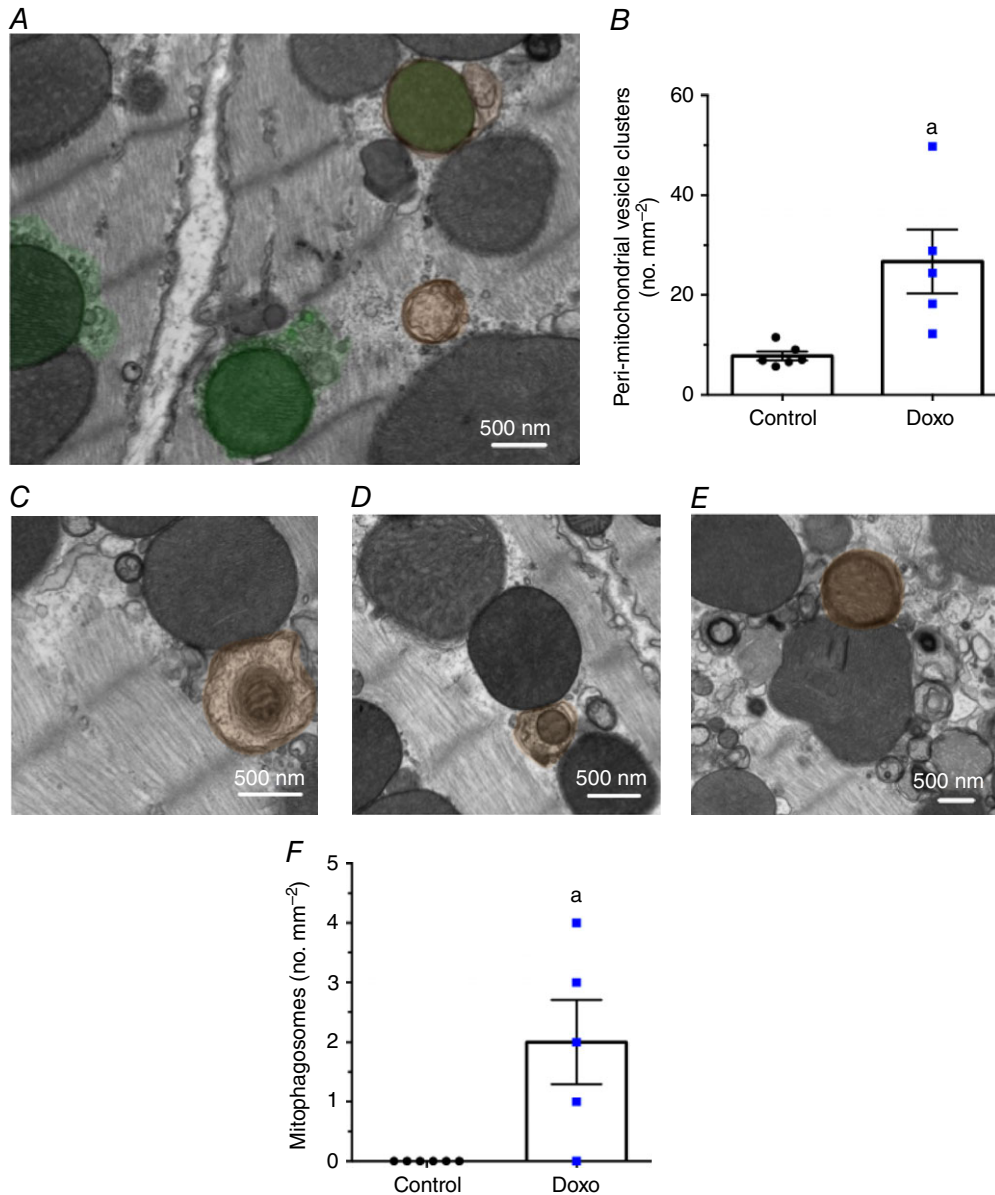


Figure 8. Increased incidence of perimitochondrial vesicular clusters and mitophagosomes in response to acute doxorubicin treatment

A, accumulation of peri-mitochondrial vesicle clusters (shaded green) in hearts from doxorubicin-treated mice. B, quantification of peri-mitochondrial vesicle clusters in control and doxorubicin-treated mice per mm² of cardiomyocyte surface area. C–E, autophagosomes containing mitochondria (shaded orange) in hearts of doxorubicin-treated mice. F, quantification of mitophagosomes in hearts from control and doxorubicin-treated mice reported per mm² of cardiomyocyte surface area. Data were obtained from the same fields of view used to quantify MDV budding events (see Fig. 7 legend for details). a, *P* < 0.05 vs. control, unpaired *t* test. Images were selected to represent average quantification data.

study, we provide further insight by direct comparison of the number of mitophagosomes and MDV budding events per cardiomyocyte surface area using the gold-standard quantitative electron microscopy approach. Under baseline conditions, from a total of 213 fields of view totalling $5000 \mu\text{m}^2$, not a single autophagosome containing mitochondria was observed, which contrasts with the comparatively higher incidence of MDV budding events detected in the same set of images. Although this represents a static view of mitophagy and MDV formation, it nevertheless highlights the relative rarity of mitochondrial engulfment into autophagosomes *vs* vesicle shedding, under normal conditions in the adult heart. However, as reported in our previous study (Piquereau *et al.* 2013), mitophagosomes were present in a quantifiable manner under pathological conditions, suggesting that mitophagy is potently induced under stress, and probably requires a mitochondrial damage threshold to be reached prior to the elimination of entire organelles. However, mitophagy also seems to play a role under physiological conditions requiring a rapid and widespread turnover of mitochondria such as during perinatal cardiac maturation, where 'fetal' mitochondria are replaced in the process of global metabolic remodelling (Gong *et al.* 2015). Altogether, these data and our previously published work (Soubannier *et al.* 2012a,b; McLelland *et al.* 2014) suggest a model in which MDV production acts as a basal

mitochondrial housekeeping mechanism and a first line of defence against stress. However, under persistent stress conditions, the MDV system could become insufficient, resulting in the accumulation of mitochondrial damage and the onset of whole organelle mitophagy. Although further work is required to validate this paradigm, it is consistent with results from recent studies showing that adult mice harbouring a germline or a cardiac-specific knockout of PARKIN have no pathological cardiac phenotype at baseline when mitophagy is impaired, but exhibit an exacerbated mitochondrial and cardiac dysfunction in response to pathological stress (Kubli *et al.* 2013; Piquereau *et al.* 2013; Song *et al.* 2015).

In summary, our data provide evidence of a dynamic MDV production system in cardiac cell mitochondria. Moreover, preliminary observations indicate that MDVs are also present in human skeletal muscle disease caused by primary mitochondrial genetic disorders (Fig. 9). Given the high degree of evolutionary conservation of mitochondrial biology across species and tissues, these findings suggest that MDV formation is likely to be a ubiquitous system that is relevant for our understanding of mitochondrial QC in the human heart. Future work identifying MDV-specific factors essential for their formation will be instrumental in determining the specific contribution of this mechanism to the maintenance of mitochondrial health.

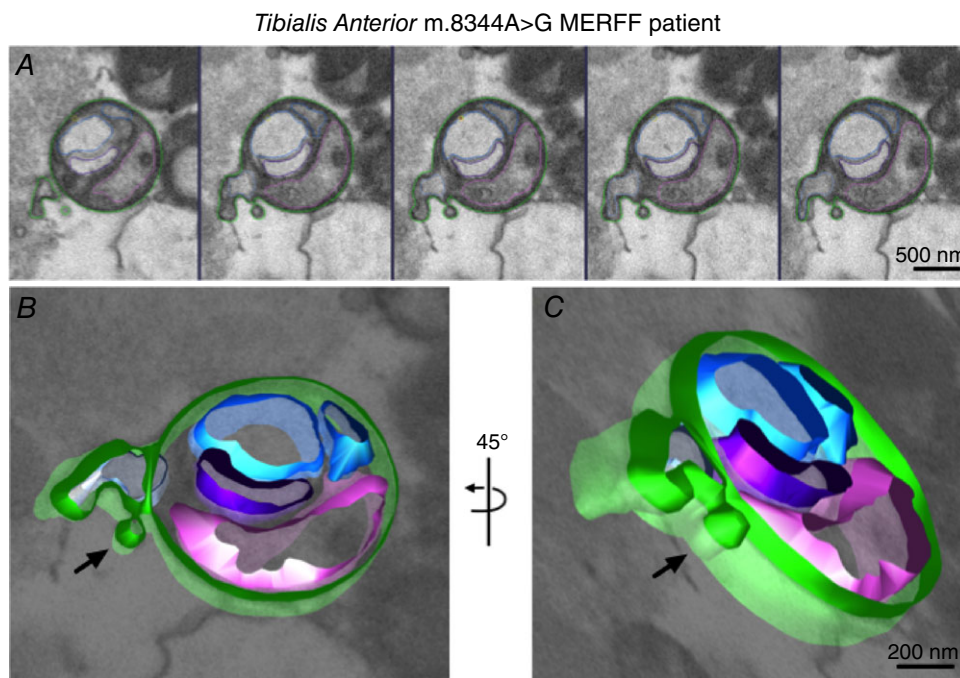


Figure 9. MDV formation in human skeletal muscle

Electron tomography (A) was performed on a biopsy of tibialis anterior from a patient possessing a mitochondrial DNA mutation of MERFF (8344A > G). The sequence of consecutive electron microscopy images showing a vesicle budding off from a mitochondria was modelled using iMod software (B, C), to better demonstrate the vesicular nature of the structure.

References

- Aries A, Paradis P, Lefebvre C, Schwartz RJ & Nemer M (2004). Essential role of GATA-4 in cell survival and drug-induced cardiotoxicity. *Proc Natl Acad Sci USA* **101**, 6975–6980.
- Ascah A, Khairallah M, Daussin F, Bourcier-Lucas C, Godin R, Allen BG, Petrof BJ, Des Rosiers C & Burelle Y (2011). Stress-induced opening of the permeability transition pore in the dystrophin-deficient heart is attenuated by acute treatment with sildenafil. *Am J Physiol Heart Circ Physiol* **300**, H1144–H1153.
- Bisetto E, Comelli M, Salzano AM, Picotti P, Scaloni A, Lippe G & Mavelli I (2013). Proteomic analysis of F1F0-ATP synthase super-assembly in mitochondria of cardiomyoblasts undergoing differentiation to the cardiac lineage. *Biochim Biophys Acta* **1827**, 807–816.
- Branco AF, Pereira SP, Gonzalez S, Gusev O, Rizvanov AA & Oliveira PJ (2015). Gene expression profiling of H9c2 myoblast differentiation towards a cardiac-like phenotype. *PLoS One* **10**, e0129303.
- Branco AF, Sampaio SF, Moreira AC, Holy J, Wallace KB, Baldeiras I, Oliveira PJ & Sardao VA (2012). Differentiation-dependent doxorubicin toxicity on H9c2 cardiomyoblasts. *Cardiovasc Toxicol* **12**, 326–340.
- Braschi E, Goyon V, Zunino R, Mohanty A, Xu L & McBride HM (2010). Vps35 mediates vesicle transport between the mitochondria and peroxisomes. *Curr Biol* **20**, 1310–1315.
- Chan NC, Salazar AM, Pham AH, Sweredoski MJ, Kolawa NJ, Graham RL, Hess S & Chan DC (2011). Broad activation of the ubiquitin-proteasome system by Parkin is critical for mitophagy. *Hum Mol Genet* **20**, 1726–1737.
- de Wit LE, Scholte HR & Sluiter W (2008). Correct assay of complex I activity in human skin fibroblasts by timely addition of rotenone. *Clin Chem* **54**, 1921–1922; author reply 1922–1924.
- Delbridge LM, Mellor KM, Taylor DJ & Gottlieb RA (2015). Myocardial autophagic energy stress responses—macroautophagy, mitophagy, and glycolysis. *Am J Physiol Heart Circ Physiol* **308**, H1194–H1204.
- Diotte NM, Xiong Y, Gao J, Chua BH & Ho YS (2009). Attenuation of doxorubicin-induced cardiac injury by mitochondrial glutaredoxin 2. *Biochim Biophys Acta* **1793**, 427–438.
- Gong G, Song M, Csordas G, Kelly DP, Matkovich SJ & Dorn GW, 2nd (2015). Parkin-mediated mitophagy directs perinatal cardiac metabolic maturation in mice. *Science* **350**, aad2459.
- Gottlieb RA & Carreira RS (2010). Autophagy in health and disease. 5. Mitophagy as a way of life. *Am J Physiol Cell Physiol* **299**, C203–C210.
- Hoshino A, Matoba S, Iwai-Kanai E, Nakamura H, Kimata M, Nakaoka M, Katamura M, Okawa Y, Ariyoshi M, Mita Y, Ikeda K, Ueyama T, Okigaki M & Matsubara H (2012). p53-TIGAR axis attenuates mitophagy to exacerbate cardiac damage after ischemia. *J Mol Cell Cardiol* **52**, 175–184.
- Hoshino A, Mita Y, Okawa Y, Ariyoshi M, Iwai-Kanai E, Ueyama T, Ikeda K, Ogata T & Matoba S (2013). Cytosolic p53 inhibits Parkin-mediated mitophagy and promotes mitochondrial dysfunction in the mouse heart. *Nat Commun* **4**, 2308.
- Kanamori H, Takemura G, Goto K, Maruyama R, Ono K, Nagao K, Tsujimoto A, Ogino A, Takeyama T, Kawaguchi T, Watanabe T, Kawasaki M, Fujiwara T, Fujiwara H, Seishima M & Minatoguchi S (2011a). Autophagy limits acute myocardial infarction induced by permanent coronary artery occlusion. *Am J Physiol Heart Circ Physiol* **300**, H2261–H2271.
- Kanamori H, Takemura G, Goto K, Maruyama R, Tsujimoto A, Ogino A, Takeyama T, Kawaguchi T, Watanabe T, Fujiwara T, Fujiwara H, Seishima M & Minatoguchi S (2011b). The role of autophagy emerging in postinfarction cardiac remodelling. *Cardiovasc Res* **91**, 330–339.
- Katajisto P, Dohla J, Chaffer CL, Pentimikko N, Marjanovic N, Iqbal S, Zoncu R, Chen W, Weinberg RA & Sabatini DM (2015). Stem cells. Asymmetric apportioning of aged mitochondria between daughter cells is required for stemness. *Science* **348**, 340–343.
- Kawaguchi T, Takemura G, Kanamori H, Takeyama T, Watanabe T, Morishita K, Ogino A, Tsujimoto A, Goto K, Maruyama R, Kawasaki M, Mikami A, Fujiwara T, Fujiwara H & Minatoguchi S (2012). Prior starvation mitigates acute doxorubicin cardiotoxicity through restoration of autophagy in affected cardiomyocytes. *Cardiovasc Res* **96**, 456–465.
- Kim I, Rodriguez-Enriquez S & Lemasters JJ (2007). Selective degradation of mitochondria by mitophagy. *Arch Biochem Biophys* **462**, 245–253.
- Koopman WJ, Visch HJ, Smeitink JA & Willems PH (2006). Simultaneous quantitative measurement and automated analysis of mitochondrial morphology, mass, potential, and motility in living human skin fibroblasts. *Cytometry A* **69**, 1–12.
- Kremer JR, Mastronarde DN & McIntosh JR (1996). Computer visualization of three-dimensional image data using IMOD. *J Struct Biol* **116**, 71–76.
- Kubli DA, Zhang X, Lee Y, Hanna RA, Quinsay MN, Nguyen CK, Jimenez R, Petrosyan S, Murphy AN & Gustafsson AB (2013). Parkin protein deficiency exacerbates cardiac injury and reduces survival following myocardial infarction. *J Biol Chem* **288**, 915–926.
- Kuznetsov AV, Javadov S, Sickinger S, Frotschnig S & Grimm M (2015). H9c2 and HL-1 cells demonstrate distinct features of energy metabolism, mitochondrial function and sensitivity to hypoxia-reoxygenation. *Biochim Biophys Acta* **1853**, 276–284.
- Lemasters JJ (2014). Variants of mitochondrial autophagy: Types 1 and 2 mitophagy and micromitophagy (Type 3). *Redox Biol* **2**, 749–754.
- Marchesi C, Essalmani R, Lemarie CA, Leibovitz E, Ebrahimian T, Paradis P, Seidah NG, Schiffrin EL & Prat A (2011). Inactivation of endothelial proprotein convertase 5/6 decreases collagen deposition in the cardiovascular system: role of fibroblast autophagy. *J Mol Med (Berl)* **89**, 1103–1111.
- Marcil M, Ascah A, Matas J, Belanger S, Deschepper CF & Burelle Y (2006). Compensated volume overload increases the vulnerability of heart mitochondria without affecting their functions in the absence of stress. *J Mol Cell Cardiol* **41**, 998–1009.
- Mastronarde DN (2005). Automated electron microscope tomography using robust prediction of specimen movements. *J Struct Biol* **152**, 36–51.

- McBride H & Scorrano L (2013). Mitochondrial dynamics and physiology. *Biochim Biophys Acta* **1833**, 148–149.
- McLelland GL, Soubannier V, Chen CX, McBride HM & Fon EA (2014). Parkin and PINK1 function in a vesicular trafficking pathway regulating mitochondrial quality control. *EMBO J* **33**, 282–295.
- Neupane B, Jin T, Mellor LF, Lobo EG, Ligler FS & Wang G (2015). Continuous-wave stimulated emission depletion microscope for imaging actin cytoskeleton in fixed and live cells. *Sensors* **15**, 24178–24190.
- Neuspiel M, Schauss AC, Braschi E, Zunino R, Rippstein P, Rachubinski RA, Andrade-Navarro MA & McBride HM (2008). Cargo-selected transport from the mitochondria to peroxisomes is mediated by vesicular carriers. *Curr Biology* **18**, 102–108.
- Picard M, Csukly K, Robillard ME, Godin R, Ascah A, Bourcier-Lucas C & Burelle Y (2008). Resistance to Ca^{2+} -induced opening of the permeability transition pore differs in mitochondria from glycolytic and oxidative muscles. *Am J Physiol Regul Integr Comp Physiol* **295**, R659–R668.
- Piquereau J, Godin R, Deschenes S, Bessi VL, Mofarrahi M, Hussain SN & Burelle Y (2013). Protective role of PARK2/Parkin in sepsis-induced cardiac contractile and mitochondrial dysfunction. *Autophagy* **9**, 1837–1851.
- Saito T & Sadoshima J (2015). Molecular mechanisms of mitochondrial autophagy/mitophagy in the heart. *Circ Res* **116**, 1477–1490.
- Song M, Gong G, Burelle Y, Gustafsson AB, Kitsis RN, Matkovich SJ & Dorn GW, 2nd (2015). Interdependence of Parkin-mediated mitophagy and mitochondrial fission in adult mouse hearts. *Circ Res* **117**, 346–351.
- Soubannier V, McLelland GL, Zunino R, Braschi E, Rippstein P, Fon EA & McBride HM (2012a). A vesicular transport pathway shuttles cargo from mitochondria to lysosomes. *Curr Biol* **22**, 135–141.
- Soubannier V, Rippstein P, Kaufman BA, Shoubridge EA & McBride HM (2012b). Reconstitution of mitochondria derived vesicle formation demonstrates selective enrichment of oxidized cargo. *PLoS One* **7**, e28230.
- Stanley WC, Recchia FA & Lopaschuk GD (2005). Myocardial substrate metabolism in the normal and failing heart. *Physiol Rev* **85**, 1093–1129.
- Sugiura A, McLelland GL, Fon EA & McBride HM (2014). A new pathway for mitochondrial quality control: mitochondrial-derived vesicles. *EMBO J* **33**, 2142–2156.
- Tokuyasu KT (1973). A technique for ultracytometry of cell suspensions and tissues. *J Cell Biol* **57**, 551–565.
- Wei H, Liu L & Chen Q (2015). Selective removal of mitochondria via mitophagy: distinct pathways for different mitochondrial stresses. *Biochim Biophys Acta* **1853**, 2784–2790.
- Willems PH, Smeitink JA & Koopman WJ (2009). Mitochondrial dynamics in human NADH:ubiquinone oxidoreductase deficiency. *Int J Biochem Cell Biol* **41**, 1773–1782.
- Zhang Y, El-Sikhry H, Chaudhary KR, Batchu SN, Shayeganpour A, Jukar TO, Bradbury JA, Graves JP, DeGraff LM, Myers P, Rouse DC, Foley J, Nyska A, Zeldin DC & Seubert JM (2009). Overexpression of CYP2J2 provides protection against doxorubicin-induced cardiotoxicity. *Am J Physiol* **297**, H37–H46.

Additional information

Competing interests

None.

Author contributions

Conception or design of the work: VJJC and YB. Acquisition, analysis, or interpretation of data for the work *and* drafting the work or revising it critically for important intellectual content: VJJC, SD, AC, FB, AV, DT, MP, HM, and YB. All authors: approved the final version of the manuscript; agreed to be accountable for all aspects of the work in ensuring that questions related to the accuracy or integrity of any part of the work are appropriately investigated and resolved; and qualified for authorship. All those who qualify for authorship are listed.

Funding

This work is funded by grants from the National Science and Engineering Research Council of Canada (NSERC) and the Canadian Institute of Health Research (CIHR) to YB. VJJC is recipient of a postdoctoral fellowship from the Fonds de Recherche Québec Santé (FRQS).

Acknowledgements

We thank the Facility for Electron Microscopy Research (FEMR), McGill University, in particular Jeannie Mui for technical support and TEM training provided. Also, a special acknowledgement to Dewight Williams from the University of Pennsylvania Electron Microscopy Resource Laboratory.